OPTICA

Electrically pumped laser transmitter integrated on thin-film lithium niobate

Amirhassan Shams-Ansari,[1,*] **Dylan Renaud,**[1] **Rebecca Cheng,**[1] **Linbo Shao,**[1] **Lingyan He,**[2] **Di Zhu,**[1] **Mengjie Yu,**[1] **Hannah R. Grant,**[3] **Leif Johansson,**[3] **Mian Zhang,**[2] **and Marko Lončar**[1,4]

[1]*John A. Paulson School of Engineering and Applied Sciences, Harvard University, Cambridge, Massachusetts 02138, USA*
[2]*HyperLight, 501 Massachusetts Avenue, Cambridge, Massachusetts 02139, USA*
[3]*Freedom Photonics, 41 Aero Camino, Goleta, California 93117, USA*
[4]*e-mail: loncar@seas.harvard.edu*
**Corresponding author: ashamsansari@seas.harvard.edu*

Received 15 November 2021; revised 9 February 2022; accepted 13 February 2022 (Doc. ID 448617); published 6 April 2022

Integrated thin-film lithium niobate (TFLN) photonics has emerged as a promising platform for the realization of high-performance chip-scale optical systems. Of particular importance are TFLN electro-optic modulators featuring high-linearity, low driving voltage and low propagation loss. However, a fully integrated system requires integration of high power, low noise, and narrow linewidth lasers on TFLN chips. Here we achieve this goal, and demonstrate integrated high-power lasers on TFLN platform with up to 60 mW of optical power in the waveguides. We use this platform to realize a high-power transmitter consisting of an electrically pumped laser integrated with a 50 GHz modulator.

https://doi.org/10.1364/OPTICA.448617

Long-haul telecommunication networks, data center optical interconnects, and microwave photonic systems rely on transmission of information using optical carriers [1,2]. The ideal transmitter for these applications should operate over a large bandwidth with a small driving amplitude, emit high optical power, have negligible insertion loss, and be cost-effective. Recently, thin-film lithium niobate (TFLN) has emerged as a platform capable of achieving nearly all of these requirements [3] using external lasers. The latter poses a major challenge to the achievable performance, complexity, and cost since it requires coupling between two discrete components. The ideal solution would integrate high-power and low-noise lasers on the TFLN photonic platform. Distributed feedback (DFB) lasers are excellent candidates for integration with TFLN because of their low cost, small footprint, and large output powers exceeding 100 mW. Such a solution would enable new architectures such as large arrays of high-power transmitters as well as unprecedented performance in optical links [4].

Here, we address this challenge by integrating DFB lasers capable of producing of 170–200 mW of optical power with TFLN integrated modulators featuring an electro-optic (EO) bandwidth in excess of 50 GHz [5,6]. The DFB laser utilizes a high-power InP-based platform which has demonstrated output powers >300 mW and has reported low relative intensity noise (RIN) < -160 dB/Hz at the C-band [4]. The DFB laser design ensures minimal free-carrier absorption, a lower voltage drop across the diode, and reduced mirror losses. This in turn results in a longer cavity length, which yields higher powers, lower linewidths, and a reduction in spatial hole burning. The DFB die was designed for flip-chipping by adding support structures that provide better mechanical stability during the bonding process. Using only passive-alignment and flip-chip thermo-compression bonding, we integrate DFB lasers with pre-fabricated TFLN chips. With the optimized overlap between the respective platform modes, we couple ∼60 mW of optical power into the TFLN waveguides.

Our integration approach [Fig. 1(a)] relies on butt coupling between DFB and TFLN waveguides. This approach allows for efficient injection of carriers through the active quantum well region, which is essential for the envisioned high-power laser operation. First, TFLN devices are fabricated [5,7] on a 600 nm thick, X-cut LN device layer that is bonded onto a 4.7 µm layer of thermally grown SiO_2 on top of Si substrate (NanoLN). The thickness of the buried oxide is chosen so that the optical mode-height of the flipped DFB laser waveguide (∼4.44 µm) and TFLN waveguide (∼5 µm) [Fig. 1(b)] are nearly matched. Mode height matching is later fine-tuned using gold deposition. The waveguide width is chosen to be 800 nm to ensure single-mode operation. The waveguides are first defined using a negative-tone electron-beam resist (FOx-16, Dow Corning). The pattern is then transferred to TFLN by reactive ion etching using Ar^+ to reach the slab height of 300 nm. We later deposit 800 nm of SiO_2 using plasma-enhanced chemical vapor deposition as a device cladding. At the coupling region, the waveguides are tapered out to 8.2 µm in width. This horn coupler geometry ensures maximal overlap with the optical mode produced by the 5 µm wide DFB laser, and features high tolerances to lateral misalignment, mode height misalignment, and separation (gap) between the DFB and TFLN waveguides [Fig. 1(c)]. In our simulation, we implement an antireflective (AR) coating of Al_2O_3 at the laser interface to match the refractive index difference of the laser mode and air, matching the AR coating of the

Corrected 6 April 2022

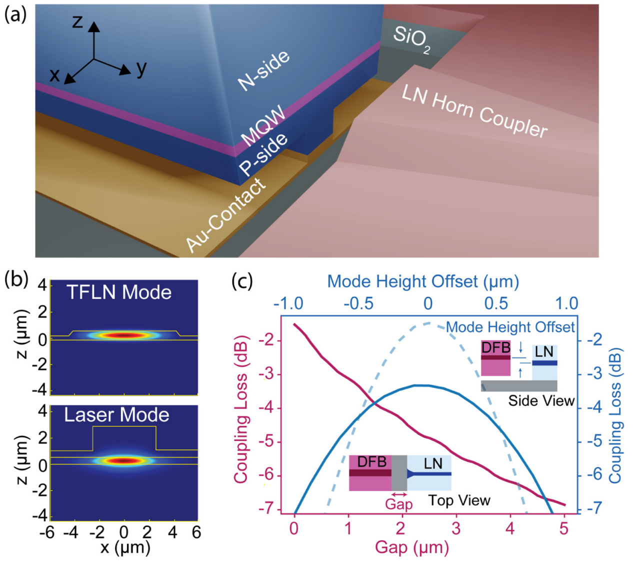

Fig. 1. Integration of DFB lasers onto TFLN: (a) An illustration of the proposed approach. The DFB laser is flipped and the height is adjusted to ensure matched mode-heights between the two waveguides. (b) Optical mode profiles for both TFLN and DFB waveguides, obtained using a finite-difference eigenmode solver. (c) Mode overlap simulations showing the coupling loss between the laser and TFLN waveguides as a function of the gap size (red) and height offset (blue). The latter are shown for gap size = 1.2 μm (solid blue) and 0 μm (dashed blue). Insets show the reference geometry for the gap and mode height offset calculation.

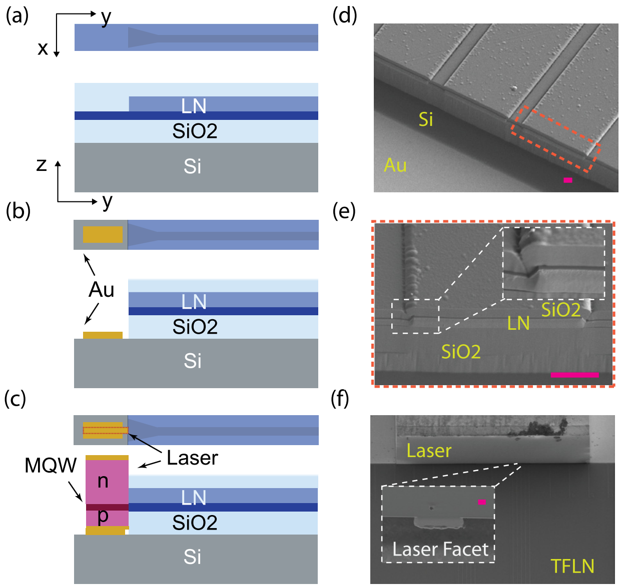

Fig. 2. Fabrication steps of the flip-chip bonding process: (a) Top-down and cross-section illustration of the initial TFLN stack. (b) A trench is patterned and etched at the tip of the horn coupler. Then, a Ti/Pt/Au bonding pad (used for bonding and carrier injection) is defined 10 μm away from the edge of the groove using a second lithography step and deposition. (c) The DFB laser is flipped and bonded to the pad using thermo-compression Au–Au bonding (Fineplacer Femto 2). (d) Scanning electron microscope (SEM) image of the LN waveguide facets after trench fabrication. (e) A close-up SEM of the TFLN horn-coupler facet prior to bonding. (f) SEM image of the DFB laser bonded to TFLN platform. Inset shows the laser facet prior to bonding. Scale bars represent 1 μm.

fabricated laser. We confirm good agreement between these simulation results and experiment by performing a separate transmission measurement using separate DFB and LN chips.

The final step in TFLN chip fabrication is the realization of a trench at the end of the horn coupler, where DFB lasers will be introduced. First, the upper SiO$_2$ cladding is etched using RIE with a mixture of C$_3$F$_8$ and Ar gases. The LN layer is subsequently etched away using the same recipe as the waveguides, followed by a buried oxide etch [Figs. 2(a)–2(c)]. Since the sidewall angle sets the minimum coupling gap between the DFB and TFLN waveguides, a smaller sidewall angle is desired to increase the coupling efficiency [Figs. 2(d) and 2(e)]. We evaluate the sidewall angle to be ~85° (currently limited by the reactive ion-etching process), which sets the minimum achievable gap between the laser and the waveguide to be ~500 nm. Finally, a Ti/Pt/Au metal layer is deposited at the bottom of the trench using electron beam evaporation. This metallic layer serves as both one of the laser electrodes and the bonding pads. The laser is flip-chip bonded, P-side down, onto the metal layer at the bottom of the trench using gold–gold thermo-compression bonding [Fig. 2(f)]. The mode height offset between the DFB and TFLN waveguides can be controlled by adjusting the thickness of the gold layer deposited in the trench.

On this passive device [Fig. 3(a)], the LIV measurements are performed by contacting a sourcemeter (Keithley 2400) to the N- and P-side of the laser and increasing the current up to 1.0 A [Fig. 3(b)]. Clear evidence of single-mode operation without mode hopping is observed for all integrated lasers tested [Fig. 3(b), inset]. The laser emission is collected from the TFLN device facet using a single lens with a numerical aperture of 0.4. Taking into account the out-coupling losses, which we measure to be 4.8 ± 0.5 dB, we estimate an on-chip optical power in the range 60 ± 7 mW at 1.0 A, under room temperature operation (no cooling). Such on-chip power is among the highest reported for all integrated photonics platforms [8–10]. We achieve a coupling loss of ~5.2 dB between the laser and TFLN waveguide which is due to sidewall slope and alignment accuracy. The coupling loss between the DFB and TFLN waveguide was evaluated in the following way: first, the maximum output power of the DFB was measured (before bonding) and found to be in the range of 170–200 mW (measured among several devices). Next, we bonded the laser and measured the output power, delivered via TFLN chip, and collected at the output side of the TFLN waveguide. This maximum output power was measured to be ~19.8 mW. This results in an overall insertion loss of ~10 dB. This is a conservative value since we assumed DFB output power of 200 mW. Next, we measured the coupling loss between the TFLN waveguide and high-NA lens to be 4.8 ± 0.5 dB, using separate devices with identical waveguide geometries. Subtracting this coupling loss from the overall insertion loss, we find the DFB–TFLN waveguide coupling loss to be 5.2 ± 0.5 dB. Finally, the DFB linewidth is measured using a delayed self-heterodyne technique and found to be below 1 MHz. This is consistent with the linewidths measured on DFB lasers before integration.

To illustrate the full potential of our approach, DFB lasers are integrated with a TFLN EO-modulator [Fig. 4(a)]. Electro-optic modulation is achieved using an integrated intensity modulator with 5 mm long segmented traveling wave electrodes [6]. We choose the segmented electrode design for the modulator to avoid higher RF loss caused by electrical current crowding in the metallic gaps while maintaining the same modulation efficiency. Segmented electrodes also offer improved velocity matching

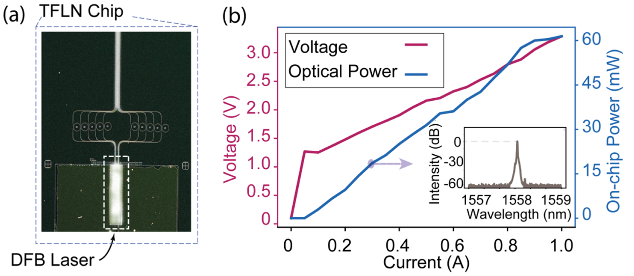

Fig. 3. Characterization of DFB laser integrated on a passive TFLN device: (a) Microscope image of an exemplary passive device with bonded DFB laser. TFLN chip features several waveguides coupled to ring resonators. (b) Optical power inside TFLN waveguide and laser voltage as a function of the laser driving current. The inset shows the lasing spectrum confirming single-mode operation. The emission wavelength of DFB is not in resonance with the ring resonator in this experiment.

between the microwave and optical fields, enabling higher operating bandwidth. A schematic of the modulator, including all design parameters, is shown in Fig. 4(b). The optical waveguide is tapered up to 1.5 µm in the interaction region to maintain low optical loss and high overlap between the optical and RF fields. Using the termination impedance ($Z_{\text{Load}} = 50\Omega$), we first extract the phase index and characteristic impedance (Z_C) to be 2.3 and 42Ω, respectively, by electrical characterization of the transmission line (S_{11} and S_{21}). We then fit the RF loss of the segmented electrodes and find the loss coefficient to be $\alpha_{\text{RF,seg}} = 0.83\ \text{dBcm}^{-1}\text{GHz}^{-1/2}$, which allows extrapolation of the electrical S_{21} up to 100 GHz [Fig. 4(c), red curve]. We predict the 3 dB bandwidth cutoff (w.r.t 1 GHz) of our modulator to be approximately 100 GHz [Fig. 4(c), blue curve] [6].

In this active device, a maximum of ∼25 mW (driving current ∼0.8 A) of optical power is estimated after the Mach–Zehnder interferometer [Fig. 4(d)]. The lower power in these active devices, compared to a passive one, can be attributed to sub-optimal alignment as well as to absorption loss introduced by metal electrodes in this modulator design that features small electrode gap (electrode gaps ∼4 µm). The latter can be easily addressed by increasing the electrode separation at the expense of reduced electro-optic efficiency. The electrodes are contacted using ground–signal–ground probes (GSG) (GGB Model 50 A) and terminated using a 50Ω termination. A measured V_π of 4.3 V demonstrates that the DFB emission can be modulated efficiently on-chip [Fig. 4(e)]. To show the full functionality of our platform as an integrated transmitter, we measure the high-frequency electro-optic response of our transmitter (S_{21}) [Fig. 4(f)]. We used a 50 GHz Vector Network Analyzer (VNA, Agilent), 45 GHz fast photo-diode (New Focus 1014), and a pair of 50 GHz GSG probes for both the electrical and the electro-optic characterizations of our transmitter. RF cable losses, probes, and detector response are subtracted from the measured frequency response. The response fluctuation beyond 45 GHz is due to the limited bandwidth of the photodiode.

In conclusion, we demonstrated to our knowledge the first high-power hybrid integrated transmitter on TFLN by flip-chip bonding a DFB laser. The bonding design allows efficient thermal anchoring for the laser, which allowed uncooled operation with up to 60 (25) mW in the passive (active) waveguides. Our high-power transmitter platform will enable a new class of applications in digital and analog communication spaces. Beyond communication systems, integrating high-power lasers on other TFLN devices such as EO [11] and Kerr combs [12,13] enables a critical step towards realizing fully integrated spectrometers [14]. Other exciting frontiers include optical remote sensing and beam-forming [15], photon pair generation [16], and efficient frequency conversion [13,17] for realization of quantum networks. Future work should focus on the realization of fully integrated photonic links through integrating high-power and high-bandwidth photodetectors on the TFLN platform [18]. Recently, another approach for integration of electrically pumped lasers and amplifiers on TFLN based on micro-transfer printing was demonstrated on TFLN [19]. While this approach has the potential for scalable integration of a large number of lasers, it may suffer from maximum achievable power and thermal stability. These issues arise from the need to use a spin-on dielectric layer, typically bisbenzocyclobutene (BCB), to planarize the surface and attach the lasers. This introduces additional thermal impedance and may affect the powers available from the laser. Furthermore, this approach relies on the lateral injection of carriers through the gain medium, which can have increased resistance, thus also limiting the available power. Moreover, it can be challenging to characterize each laser before the transfer, which can negatively impact the overall yield of the process.

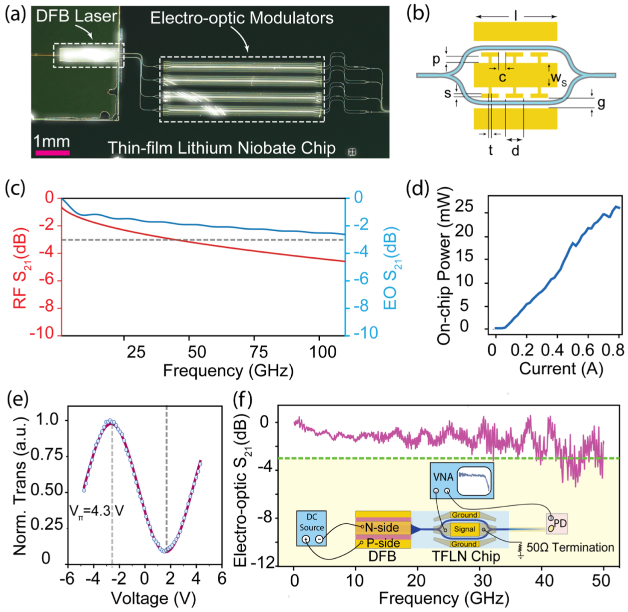

Fig. 4. Electrically pumped integrated laser-modulator transmitter: (a) Optical image of the transmitter, consisting of a DFB laser and EO intensity modulators. (b) Schematic of the segmented electrode modulator. Design parameters $(p, l, s, w_s, g, d, t, c) = (2, 5000, 2, 22, 4, 50, 10, 3)\mu\text{m}$. (c) Fitted electrical S_{21} of the modulator (red curve) and estimated electro-optic S_{21} (blue curve). (d) Power in TFLN waveguide versus laser current for the device pictured in (a). (e) Normalized optical transmission versus the voltage applied to the modulator. Red line corresponds to fit, with $V_\pi = 4.3$ V. (f) Small-signal electro-optic response of a device with an active modulation length of 5 mm and a 3 dB bandwidth of ∼50 GHz. S_{21}, transmission coefficient of the scattering matrix.

Funding. Defense Advanced Research Projects Agency (DARPALUMOS) (HR0011-20-C-0137); Air Force Office of Scientific Research (AFOSR) (FA9550-19-1-0376).

Acknowledgment. We acknowledge assistance from Mehdi Rezaee, Tomas Stuopis, Dmitry Padrubny, Prashanta Kharel, Kevin Luke, Christian Reimer, Sophie Weiyi Ding, Daniel Getega, and Neil Sinclair. Device fabrication was performed at the Center for Nanoscale Systems (CNS) at Harvard University.

Disclosures. L.H., M.Z., and M.L. are involved in developing lithium niobate technologies at HyperLight Corporation. H.G. and L.J. are involved in developing DFB lasers at Freedom Photonics.

Disclaimer. The views, opinions, and/or findings expressed are those of the author and should not be interpreted as representing the official views or policies of the Department of Defense or the U.S. Government.

Data availability. Data underlying the results presented in this paper are not publicly available at this time but may be obtained from the authors upon reasonable request.

REFERENCES

1. P. J. Winzer, D. T. Neilson, and A. R. Chraplyvy, Opt. Express **26**, 24190 (2018).
2. K. Kikuchi, J. Lightwave Technol. **34**, 157 (2015).
3. D. Zhu, L. Shao, M. Yu, R. Cheng, B. Desiatov, C. Xin, Y. Hu, J. Holzgrafe, S. Ghosh, A. Shams-Ansari, E. Puma, N. Sinclair, C. Reimer, M. Zhang, and M. Lončar, Adv. Opt. Photon. **13**, 242 (2021).
4. L. Johansson, G. Morrison, B. Buckley, M. Woodson, S. Estrella, K. Hay, and M. Mashanovitch, in *IEEE Research and Applications of Photonics in Defense Conference (RAPID)* (IEEE, 2019), pp. 1–2.
5. C. Wang, M. Zhang, X. Chen, M. Bertrand, A. Shams-Ansari, S. Chandrasekhar, P. Winzer, and M. Lončar, Nature **562**, 101 (2018).
6. P. Kharel, C. Reimer, K. Luke, L. He, and M. Zhang, Optica **8**, 357 (2021).
7. M. Zhang, C. Wang, R. Cheng, A. Shams-Ansari, and M. Lončar, Optica **4**, 1536 (2017).
8. M. Theurer, M. Moehrle, A. Sigmund, K.-O. Velthaus, R. Oldenbeuving, L. Wevers, F. Postma, R. Mateman, F. Schreuder, D. Geskus, K. Wörhoff, R. Dekker, R. G. Heideman, and M. Schell, IEEE Photon. Technol. Lett. **31**, 273 (2019).
9. D. Huang, M. A. Tran, J. Guo, J. Peters, T. Komljenovic, A. Malik, P. A. Morton, and J. E. Bowers, Optica **6**, 745 (2019).
10. D. Kharas, J. J. Plant, W. Loh, R. B. Swint, S. Bramhavar, C. Heidelberger, S. Yegnanarayanan, and P. W. Juodawlkis, IEEE Photon. J. **12**, 1 (2020).
11. M. Zhang, B. Buscaino, C. Wang, A. Shams-Ansari, C. Reimer, R. Zhu, J. M. Kahn, and M. Lončar, Nature **568**, 373 (2019).
12. Y. He, Q.-F. Yang, J. Ling, R. Luo, H. Liang, M. Li, B. Shen, H. Wang, K. Vahala, and Q. Lin, Optica **6**, 1138 (2019).
13. C. Wang, C. Langrock, A. Marandi, M. Jankowski, M. Zhang, B. Desiatov, M. M. Fejer, and M. Lončar, Optica **5**, 1438 (2018).
14. A. Shams-Ansari, M. Yu, Z. Chen, C. Reimer, M. Zhang, N. Picqué, and M. Lončar, "An integrated lithium-niobate electro-optic platform for spectrally tailored dual-comb spectroscopy," arXiv preprint arXiv:2003.04533 (2020).
15. P. A. Morton and M. J. Morton, J. Lightwave Technol. **36**, 5048 (2018).
16. J. Zhao, C. Ma, M. Rüsing, and S. Mookherjea, Phys. Rev. Lett. **124**, 163603 (2020).
17. J. Lu, M. Li, C.-L. Zou, A. Al Sayem, and H. X. Tang, Optica **7**, 1654 (2020).
18. Y. Wang, Z. Wang, Q. Yu, X. Xie, T. Posavitz, M. Jacob-Mitos, A. Ramaswamy, E. J. Norberg, G. A. Fish, and A. Beling, IEEE J. Sel. Top. Quantum Electron. **24**, 6000206 (2018).
19. C. O. de Beeck, F. M. Mayor, S. Cuyvers, S. Poelman, J. F. Herrmann, O. Atalar, T. P. McKenna, B. Haq, W. Jiang, J. D. Witmer, G. Roelkens, A. H. Safavi-Naeini, R. V. Laer, and B. Kuyken, Optica **8**, 1288 (2021).